Highly enhanced visible light photocatalysis and in situ FT-IR studies on Bi metal@defective BiOCl hierarchical microspheres

Hong Wang[a], Wendong Zhang[b], Xinwei Li[a], Jieyuan Li[c], Wanglai Cen[c], Qiuyan Li[a], Fan Dong[a],*

[a] Chongqing Key Laboratory of Catalysis and New Environmental Materials, College of Environment and Resources, Chongqing Technology and Business University, Chongqing 400067, China
[b] Chongqing Key Laboratory of Inorganic Functional Materials, Department of Scientific Research Management, Chongqing Normal University, Chongqing, 401331, China
[c] College of Architecture and Environment, Institute of New Energy and Low Carbon Technology, Sichuan University, Chengdu, Sichuan 610065, China

ARTICLE INFO

ABSTRACT

3D plasmonic Bi metal@defective BiOCl hierarchical microspheres were constructed by a one-step solvothermal method. The effects of solvent thermal temperature on the microstructure and the photocatalytic performance were investigated. The photocatalyst prepared at 200 °C (Bi/BiOCl-200) showed most efficient visible photocatalytic activity for NOx removal. The enhanced activity can be ascribed to synergistic effects of oxygen vacancies and Bi metals. The oxygen vacancies in BiOCl induce the formation of an intermediate level to allow electrons transition from the valence band to intermediate level and then to the conduction band as revealed by density functional theory (DFT). The surface plasmon resonance (SPR) effect of elemental Bi enables the improvement of the visible light absorption efficiency and the promotion of the charge carrier separation as evidenced from the charge difference distribution between Bi atoms and Bi-O layers in BiOCl. The NO adsorption and reaction processes on Bi/BiOCl-200 were dynamically monitored by in situ infrared spectroscopy (FTIR). The mechanism of Bi metals and oxygen vacancies co-mediated photocatalytic performance on Bi/BiOCl was proposed based on the results of intermediate products analysis, radicals trapping and DFT calculation. The present work could provide new insights into the mechanistic understanding of the non-noble metal Bi-based plasmonic photocatalysts and offer a new technique to reveal the mechanism of gas-phase photocatalytic reaction.

1. Introduction

Bi-based photocatalysts have been widely investigated because of their unique electronic structure and decent photocatalytic properties. The currently reported Bi-based semiconductor photocatalysts include Bi_2O_3 [1,2], Bi_2WO_6 [3–5], Bi_2MoO_6 [6–8], $(BiO)_2CO_3$ [9,10], BiOX (X = I, Br, Cl) [11–13] and so on. Various modification methods (such as formation of heterojunction [14,15], doping [16,17], etc.) are applied to further improve the photocatalytic activity of Bi-based semiconductors. Compared with the Bi-containing compounds, the elemental Bi has a low effective mass, an average free path and a high carrier activity. In comparison with noble metals (Au, Ag), Bi element also demonstrates the SPR property, but has the advantage of low cost and easy availability [18,19]. Therefore, the Bi metal as a cheap non-noble metal-based plasmonic element has received increasing research interests.

Recently, Dong et al. found that elemental Bi could demonstrate a direct plasmonic photocatalytic performance [20]. Subsequently, it is used as a co-catalyst to improve the photocatalytic properties of other semiconductors, such as Bi/TiO_2 [21], $Bi/g-C_3N_4$ [22], $Bi/(BiO)_2CO_3$ [23], $Bi/BiWO_6$ [24], Bi/BiOI [25] and other Bi-based composite photocatalysts. Song et al. [26]. prepared Bi/BiOCl heterojunction exhibiting excellent photocatalytic activity due to enhanced electron-hole separation efficiency. Liu et al. [27]. deposited elemental Bi on the surface of BiOCl nanosheet by in situ reduction method to improve the photocatalytic activity. Dong et al. [28]. constructed the Bi nanowires@ BiOCl nanosheets composites photocatalyst and proposed the mechanism of the Bi element in enhancing the plasmonic photocatalysis from the aspects of crystal surface exposure and defects. However, the specific role of oxygen vacancies and the reaction mechanism of visible photocatalytic purification of NO on Bi/BiOCl have not been elucidated. Also, Bi/BiOCl with a three-dimensional (3D) hierarchical structure has not been reported.

In the present work, Bi elements decorated defective BiOCl hierarchical microspheres were prepared by a facile solvothermal method. The in situ formation of Bi metals and oxygen vacancies in BiOCl can be

achieved simultaneously. The effects of solvothermal temperature were systematically studied. The band structure, electronic structure and electron transfer pathway in Bi/BiOCl was calculated with DFT. The photocatalytic NO oxidation mechanism with the Bi/BiOCl was investigated by in situ FT-IR. The Bi metals and oxygen vacancies co-mediated photocatalysis mechanism on Bi/BiOCl was proposed for the first time. This work could provide a new understanding of the development of non-noble metal-based (Bi-based) plasmonic photocatalyst and a new way to reveal the mechanism of gas-phase photocatalytic reaction.

2. Experimental

2.1. Sample preparations

The chemical reagents used in this experiment were analytical grade. The preparation process is as follows: 1.94 g of bismuth nitrate $(Bi(NO_3)_3 \cdot 5H_2O)$ and 50 mL of ethylene glycol were added in a water autoclave, stirring to dissolve. Then, 0.30 g of potassium chloride was dissolved in ethylene glycol (20 mL) and added to bismuth nitrate solution, stirring continued for 30 min. The mixture transferred into a 100 mL Teflonlined stainless autoclave for solvent thermal reaction (100 °C, 12 h). After the mixture cooled to room temperature, the obtained sample was washed (twice with water and twice with ethanol) and dried (60 °C) to obtain the final product labeled BiOCl-100. Under the same conditions, the solvothermal temperature was set as 180, 200 and 210 °C, and the final products were labeled Bi/BiOCl-180, Bi/BiOCl-200, Bi/BiOCl-210.

2.2. Characterization

The crystal structure of the sample was analyzed by X-ray diffraction with Cu Kα (XRD, Model D/Max RA, Rigaku Co., Japan). X-ray photoelectron spectroscopy (XPS, Thermo ESCALAB 250, USA) analyzed the chemical composition of the sample. Scanning electron microscopy (SEM. JEOL Model JSM-6490, Japan) characterized the morphology of the sample. N_2 adsorption-desorption instrument (ASAP 2020, USA) measured the specific surface area (BET) and the pore structure of the sample. UV–vis DRS (UV2550, Shimadzu) and photoluminescence spectra (PL, F-7000, Hitachi, Japan) were utilized to analyze the optical properties of the samples. The electron paramagnetic resonance (EPR) measurements of samples were performed at 77 K (FLsp920, England).

2.3. Evaluation of visible light photocatalytic activity

The photocatalytic activity was evaluated by monitoring the concentration of ppb grade NO in a continuous stream reactor at room temperature. 0.1 g of the sample was ultrasonically dispersed in a 12 mm diameter glass disk and dried at 60 °C. After natural cooling, the mixture was placed in a rectangular reactor with a capacity of 4.5 L (30 cm × 15 cm × 10 cm), covered with a layer of quartz glass and a 150 W commercial halogen tungsten lamp placed vertically above the reactor 20 cm. For visible light catalytic activity tests, filters were used to remove less than 420 nm of light from the beam. A low concentration of NO was prepared using standard air and NO standard gases with an original concentration of 100 ppm (1 ppm = 1 mg/m³). The air flow rate was 2.4 L/ min and the NO gas flow rate was 15 mL/ min. The air flow and the NO gas stream were mixed by means of a three-way valve to obtain an initial concentration of 600 ppb of NO. The diluted NO was passed into the reactor, and the NO concentration was stabilized and the lamp was turned on. The NOx analyser (Thermo Scientific, 42i-TL, USA) sampled every 1 min and recorded the concentrations of NO, NO_2 and NOx (NO + NO_2). The removal rate (η) of NO can be calculated as follows:

$$\eta \ (\%) = (1 - C/C_0) \times 100\%$$

Where, C represents the NO concentration at the outlet of the reactor after turning on the lamp, and C_0 represents the NO concentration when the adsorption-desorption equilibrium is reached before turning on the lamp.

2.4. Simulation of electromagnetic field distribution

Based on the finite integral technique, the field distribution of the Bi nanosphere was simulated by a strict Maxwell solver [29]. The time-harmonic inverse iterative method overcame the instability of the negative properties of metal [30]. The implementation of this method was parallelized to handle the large amount of freedom required for simulations of multiple structures involving plasmonic effects [31]. The computational domain is the sphere. The axis of the Bi nanospheres is located in the centre x-y plane, and the periphery is free space. Apply the perfect matching layer on all edges to truncate the calculation area. The refractive index of Bi in the visible spectrum is obtained by fitting the Drude model of empirical data [32]. The refractive index of Bi is 1.9753. The refractive index of BiOCl is 2.150. Bi nanosphere has a diameter of 400 nm.

2.5. DFT calculations

Spin-polarized DFT-D2 [33] calculations were carried out utilizing the "Vienna ab initio simulation package" (code VASP5.4) [34,35], using a universal gradient correlation functional [36]. A plane-wave basis set with energy cut off at 400 eV with the framework of the projector-augmented wave method was adopted. The Gaussian smearing width was set to 0.2 eV [37,38]. The Brillouin zone was sampled with a 3 × 3 × 1 K points. All atoms were allowed to converge to 0.01 eV $Å^{-1}$ A 15 × 15 × 23 supercell of BiOCl including 64 oxygen atoms, 48 bismuth atoms and 48 Cl atoms was employed first. Then 10 Bi atoms were supported on the surface of BiOCl [39,40].

2.6. In situ DRIFTS investigation on photocatalytic NO oxidation

In situ infrared test equipment was composed of Tensor II FTIR spectrometer (Bruker) and in-situ reflection reaction (Fig. 1). The catalyst was loaded in the reaction chamber. The real-time FTIR spectrum after heat treatment was utilized as background. The reaction gas (50 mL/min NO, 50 mL/min O_2) was then passed into the reaction chamber. After 20 min of adsorption, the catalyst was irradiated with visible light for 60 min. At the time of adsorption and reaction, the IR spectrum data was recorded every 2 min. Among 4000–600 cm^{-1} of infrared scanning range, 2200–800 cm^{-1} can be used to analyse the process of Bi-BiOCl adsorption and photocatalytic oxidation of NO.

3. Results and discussion

3.1. Phase and composition

Fig. 2a shows the XRD patterns of BiOCl-100 and Bi/BiOCl-X (X = 180, 200, 210). It can be observed that the diffraction peaks of BiOCl-100 belong to tetragonal phase BiOCl (JCPDS-ICDD Card No.06-0249). With the increase of the reaction temperature, the diffraction peaks of the Bi element (JCPDS-ICDD Card No.44-1246) begin to appear and the intensity is gradually intensified from 180 to 210 °C. Bi content of Bi/BiOCl-180 is too low to show the characteristic peaks of the Bi element in the XRD pattern. These results indicate that part of the Bi^{3+} in BiOCl is in-situ reduced to Bi elements by ethylene glycol in the solvent thermal treatment process. It is noteworthy that the diffraction peaks of BiOCl in Bi/BiOCl-X do not change after Bi deposition, indicating that the Bi elements are present only on the surface of BiOCl without changing the crystal structure of BiOCl. Fig. S1 shows that Bi/
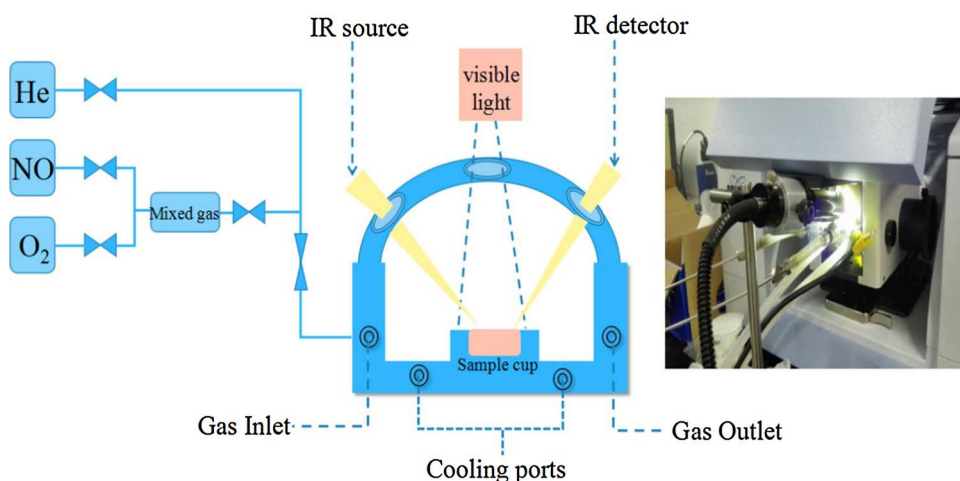
BiOCl-200 contains Bi, O, C and Cl elements. Among them, C 1 s come from adventurous carbon from the apparatus. The binding energy at 164.5 eV (Bi4f$_{5/2}$) and 159.2 eV (Bi4f$_{7/2}$) can be attributed to Bi^{3+} [41], and the binding energy of 162.2 eV (Bi4f$_{5/2}$) and 156.9 eV (Bi4f$_{7/2}$) belong to Bi element [42,43]. The metal Bi content is increased with the increasing solvothermal temperature (Table 3). This result is consistent with the XRD, further confirming that the elemental Bi is formed when the solvothermal temperature increased to 200 °C. In Fig. 2c, two dominant peaks located at 198.2 eV and 199.9 eV can be assigned to Cl 2p$_{3/2}$ and Cl 2p$_{1/2}$, respectively. In Fig. 2d, the peak at 530.3 eV belongs to the Bi−O bond [44,45].

3.2. Morphology and structure

Fig. 3a–h shows the SEM images of BiOCl-100 and Bi/BiOCl-X. Fig. 3a and b show that BiOCl-100 is self-assembled compactly by nanosheets to form hierarchical microspheres. The size of the microspheres is 1.0–3.0 μm. When the reaction temperature is raised to 180 °C, as shown in Fig. 3c and d, the thickness of the nanosheets is increased and the microsphere size becomes to be 1.0–4.0 μm. From Fig. 3e and f, it can be seen that when the temperature rises to 200 °C, the hierarchical microsphere structure of the sample is preserved, but the nanosheets become fluffier. The inserted SEM image in Fig. 3e clearly display the Bi metal is deposited on the BiOCl hierarchical microsphere. Fig. 3g and h demonstrate that when the temperature reaches 210 °C, the hierarchical microspheres are collapsed and the nanosheets are randomly assembled. The element mapping of BiOCl-100 and Bi/BiOCl-X also is shown in Figs. S2–S5. It can be seen that the Bi metal is uniformly distributed across the sample. The corresponding diagram of the Bi/BiOCl-200 is illustrated in Fig. 3i and TEM image (Fig. 3j) further demonstrates that Bi/BiOCl-200 is self-assembled by thin-layer nanosheets. Fig. 3k shows the HRTEM image of a single
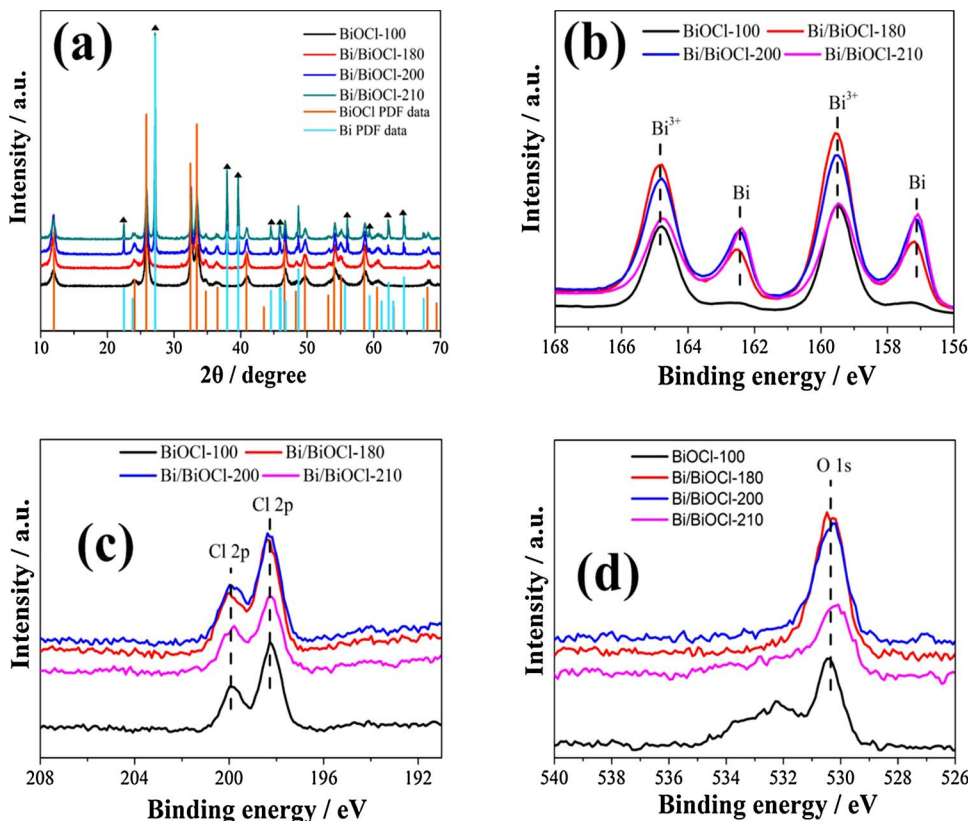

Fig. 2. XRD patterns of BiOCl-100, Bi/BiOCl-X (X = 180, 200, 210) (a), ▲ Symbol represents the diffraction peaks of Bi metal. XPS spectra of BiOCl-100 and Bi/BiOCl-X (b) Bi 4f, (c) Cl 2p and (d) O 1s.
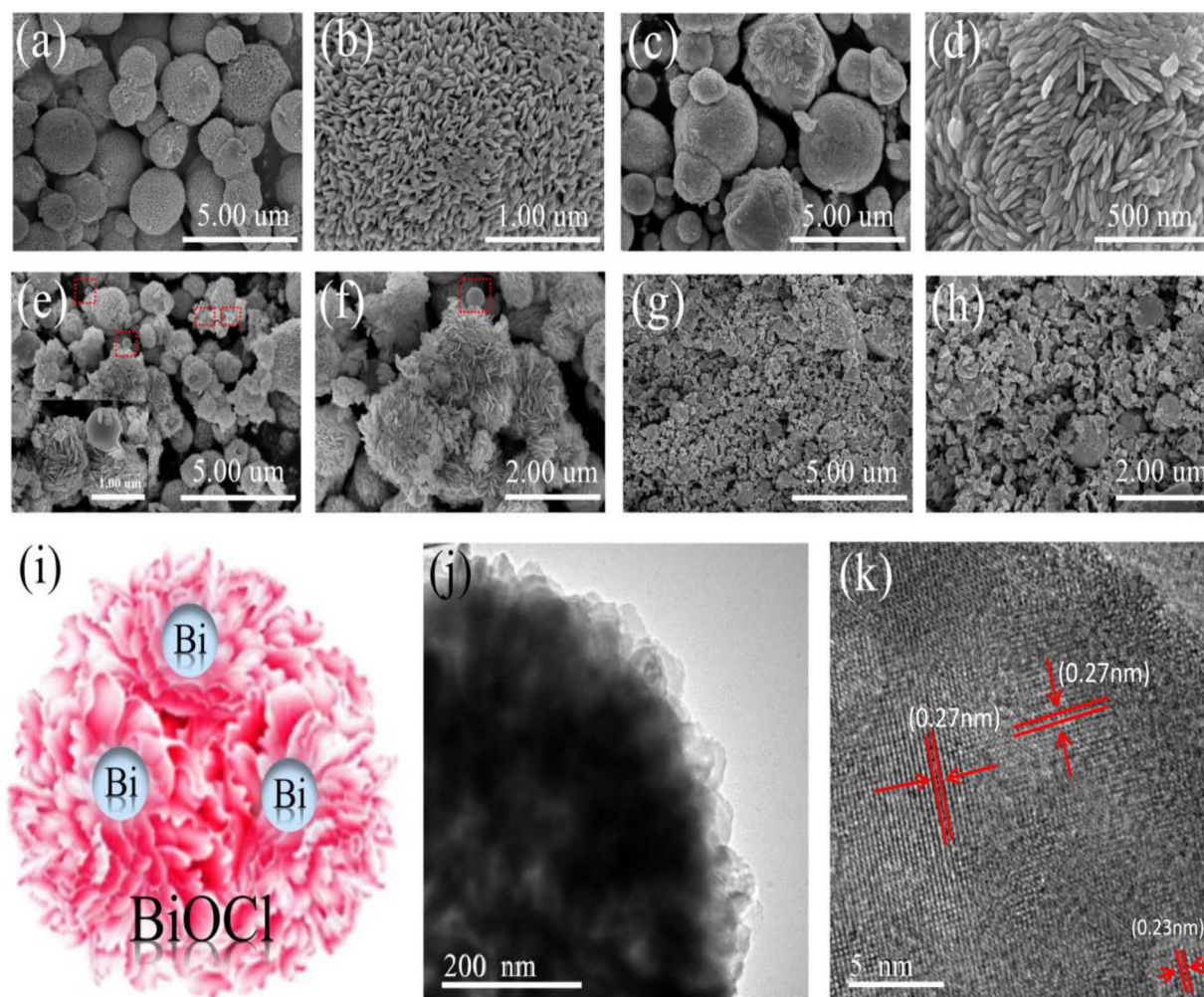
Fig. 3. SEM images of Bi/BiOCl-100 (a,b), Bi/BiOCl-180 (c,d), Bi/BiOCl-200 (e,f) and Bi/BiOCl-210 (g, h); diagram (i), TEM (j) and HRTEM (k) images of Bi/BiOCl-200.

nanosheet. The lattice spacing (0.27 nm and 0.23 nm) can be observed, corresponding to the (110) crystal plane of BiOCl and the (110) plane of Bi [27,28].

Fig. 4a and b show the N_2 adsorption-desorption isotherms and corresponding pore sizes of BiOCl-100 and Bi/BiOCl-X. According to the Brunauer-Deming-Deming-Teller (BDDT) classification, the above samples belong to the IV isotherm, indicating the presence of mesopores in the sample (Fig. 4a). The hysteresis loop of the adsorption-desorption isotherms can be classified as H3 (classified by IUPAC), indicating the presence of fractured pores due to the stacking of

nanosheets, consistently with the SEM results (Fig. 3a–h). From the pore size distribution curve (Fig. 4b), the pore sizes of the samples BiOCl-100 and Bi/BiOCl-X located at 4–20, 2–60, 2–80 and 2–140 nm, respectively, which further confirm the formation of mesoporous structure (2–50 nm). As the reaction temperature is increased to 200 °C, the fluffy stacking of nanosheets is the main reason for the formation of large pores and enlarged specific surface areas. Table 1 show the specific surface area and the pore volume of the samples increased from 12 to 18 m^2/g and 0.051–0.110 cm^3/g, respectively, as the reaction temperature increased from 100 to 200 °C. However, when the
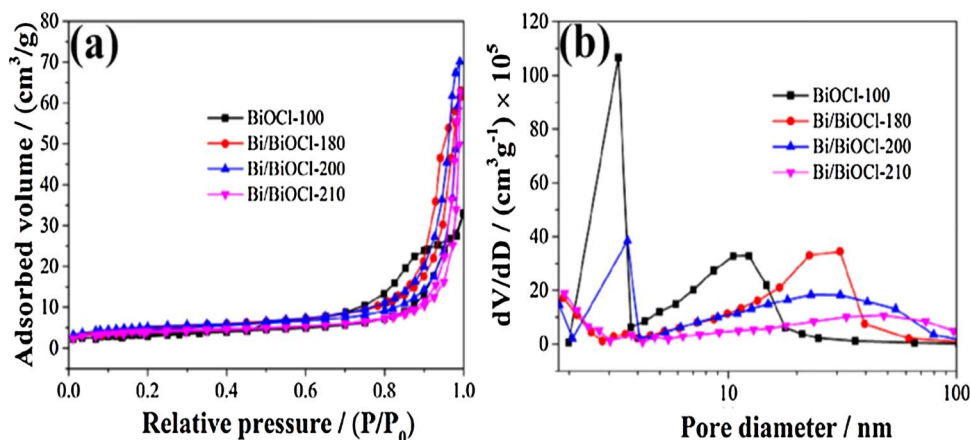

Fig. 4. N_2 adsorption-desorption isotherms (a) and pore size distribution curves (b) of BiOCl-100 and Bi/BiOCl-X (X = 180, 200, 210).

Table 1
The surface area, pore parameter and NO removal ratio of the samples.

Sample	BET (m^2/ g)	Pore Volume (cm^3/ g)	$\eta_{(NO)}$ (%)
BiOCl-100	12	0.051	48.4
Bi/BiOCl-180	17	0.097	61.0
Bi/BiOCl-200	18	0.110	67.5
Bi/BiOCl-210	14	0.096	58.6

temperature was increased to 210° C, the specific surface area and pore size of the samples are reduced, which is caused by the collapse of the hierarchical structure (Fig. 3g and h).

3.3. Light absorption and oxygen vacancy

Fig. 5a displays the UV–vis diffuse reflectance spectra of BiOCl-100 and Bi/BiOCl-X. We can observe that the BiOCl-100 already show an extended light absorption up to 500 nm, which is different from the intrinsic light absorption of BiOCl in the UV region. Besides, the band gap of the BOCl-100 estimated from the intercept of the tangents to the plots of $(\alpha h\nu)^{1/2}$ νs photoenergy (Fig. 5b) is 3.16 eV, which make the BOCl hardly absorb visible adsorption. This contradiction may be caused by the presence of oxygen vacancies that modify the band structure of pristine BiOCl. Therefore, solid-state EPR spectra are recorded to demonstrate the existence of the oxygen vacancies. As shown in Fig. 5c, BiOCl-100 has a strong signal peak at g = 1.996 in the dark, which is attributable to oxygen vacancies [46,47]. At the same time, the signals of Bi/BiOCl-X gradually become stronger with the increase of the solvothermal temperature, indicating the production of increased amount of oxygen vacancies. The production of oxygen vacancies in BiOCl can be ascribed to the reductive effect of ethylene glycol [41]. Under visible light irradiation, the production of photogenerated radicals of the BiOCl-100 and Bi/BiOCl-X enhanced intensity of EPR signal [48,49]. The density of states (DOS) of intrinsic BOCl and the defective BOCl (Fig. 5d) are calculated to further reveal the role of oxygen vacancy. An obvious intermediate level (named β) is appeared under

conduction band bottom of the BOCl, implying that the oxygen vacancies contribute to the formation of intermediate level, which could achieve electrons transition from valence band (VB) to conduction band (CB) through intermediate level under visible light irradiation [28,50]. With the increase of solvothermal temperature, the reduction ability of ethylene glycol is enhanced, and thus the increased amount of Bi element and oxygen vacancies are produced [51–53]. As a result, the Bi/BiOCl-X exhibit a full absorption phenomenon in the visible region due to the SPR effect of the Bi elements, consistent with the change in the colour of the sample from light yellow to black [18,20,28].

3.4. Charge carriers separation and highly enhanced visible light photocatalytic activity

Fig. 6a shows the photoluminescence (PL) spectra for all the samples. The PL intensity of Bi/BiOCl-X is significantly lower than that of BiOCl-100. This is because the Bi elements of Bi/BiOCl-X induce the electromagnetic field through the SPR effect that could promote the separation of photogenerated charge carriers [54]. To demonstrate the existence of the SPR effect of the Bi nanosphere alone and the Bi nanosphere using BiOCl as the substrate, we simulate the electromagnetic field with a rigorous Maxwell solver based on finite integration techniques as showed in Figs. S6 and 6 b [30,31]. The electromagnetic field can be observed on both sides of the Bi nanosphere under visible light irradiation. In comparison with situation of single Bi metal, the combination Bi metal with BiOCl could enhance the SPR-induced local electromagnetic field. Fig. 6c shows the visible light photocatalytic NO removal ratio by BiOCl-100 and Bi/BiOCl-X under visible light. It can be seen that BiOCl-100 exhibits a decent 48.4% NO removal ratio after irradiation for 30 min, consistent with the phenomenon of defect-induced visible light absorption (Fig. 5a). When the preparation temperature increased from 180 to 200 °C, the NO removal ratio of Bi/BiOCl-180 and Bi/BiOCl-200 is increased to 61.0 and 67.5%, respectively, which is much more efficient than that of Bi/BiOCl without 3D structure [28]. The highly enhanced visible light photocatalysis of 3D Bi/BiOCl-200 can be ascribed to the synergistic effects of oxygen vacancies and the Bi metals. On the one hand, oxygen vacancies favour
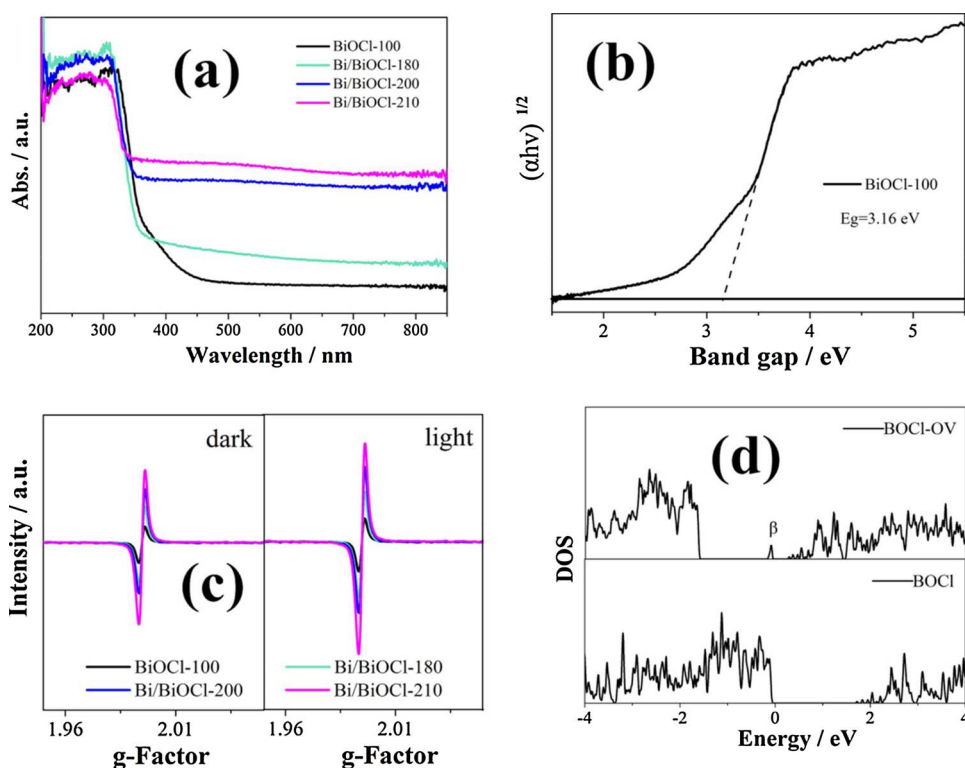

Fig. 5. UV–vis DRS (a), the band gap determination (b), EPR (c) of BiOCl-100 and Bi/BiOCl-X (X = 180, 200, 210) and (d) density of state (DOS) of BiOCl-100.
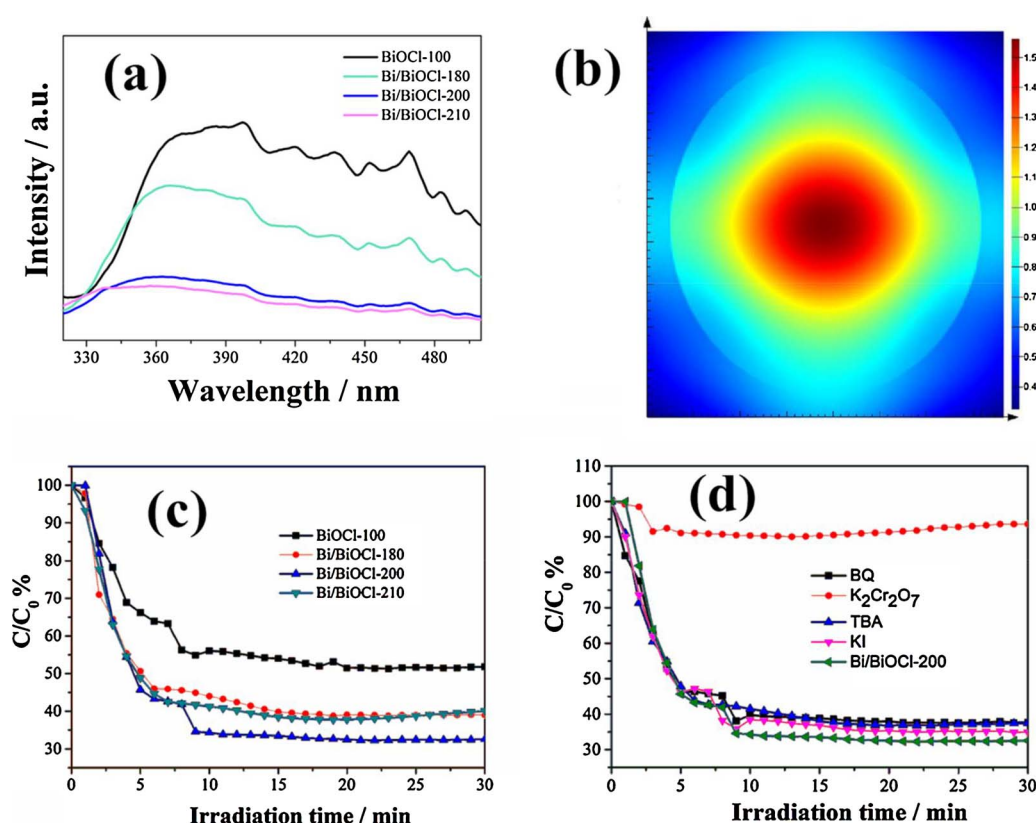
Fig. 6. PL spectra of BiOCl-100 and Bi/BiOCl-X (X = 180, 200, 210) (a); SPR-induced local electromagnetic field in the Bi nanoparticles using BiOCl as the substrate, the Bi particle is illuminated by plane waves with a wavelength of 420 nm that occur from the z-direction (b); visible light photocatalytic activity for the removal of NO in air of BiOCl-100 and Bi/BiOCl-X (X = 180, 200, 210) (c); the trapping of the radicals of Bi/BiOCl-200 during photocatalysis (d).
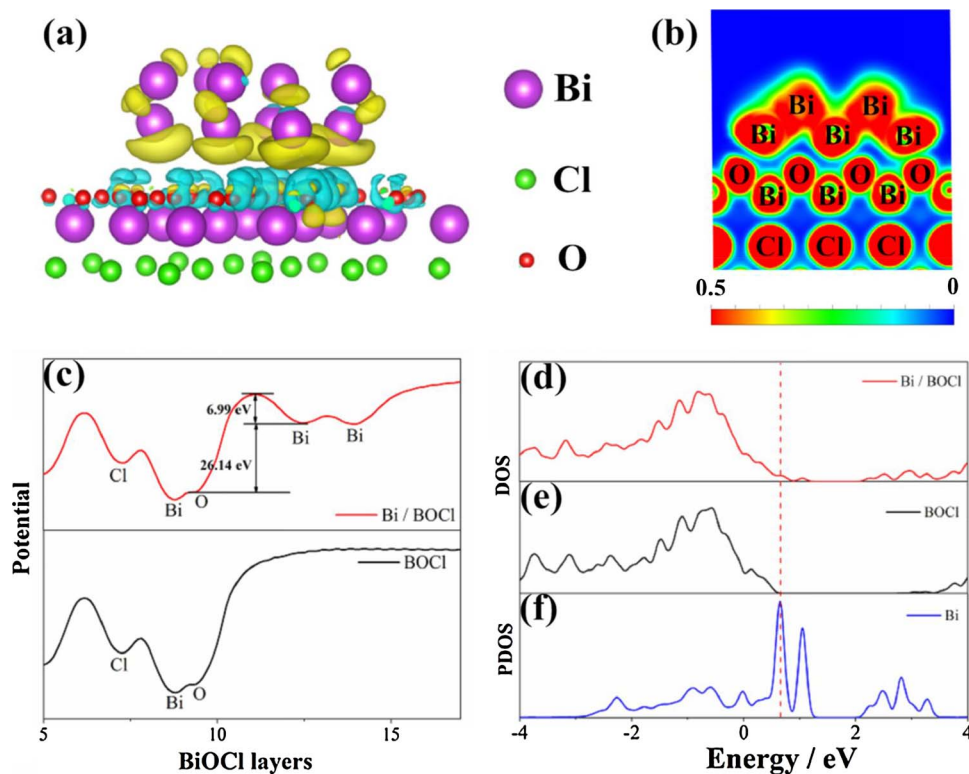

Fig. 7. Charge difference distribution between Bi atoms and Bi-O layers of the BiOCl (a): charge accumulation is in blue and depletion in yellow; electronic location function (ELF) (b); electrostatic potential (c); density of state of Bi/BiOCl (d); density of state of BiOCl (e); projected density of states (PDOS) of Bi atom in elemental Bi layers (f). (For interpretation of the references to colour in this figure legend, the reader is referred to the web version of this article.)

the transition of electrons from the valence band to an intermediate level and then to the conduction band under visible light irradiation [28,50]. On the other hand, the SPR effect of Bi elements could improve the visible light absorption efficiency (Fig. 5a) and promote the separation of photogenerated electron-hole pairs (Fig. 6a). The Bi/BiOCl-210 exhibits the strongest light absorption and higher photogenerated

charge separation efficiency. However, the hierarchical microsphere structure of Bi/BiOCl-210 is collapsed under a higher temperature treatment, resulting in a decrease in the specific surface area and thus reduction in visible light photocatalytic performance. The visible photocatalytic cycling test of Bi/BiOCl-200 is shown in Fig. S7. The catalyst showed slight deactivation after five recycled runs probably due to the
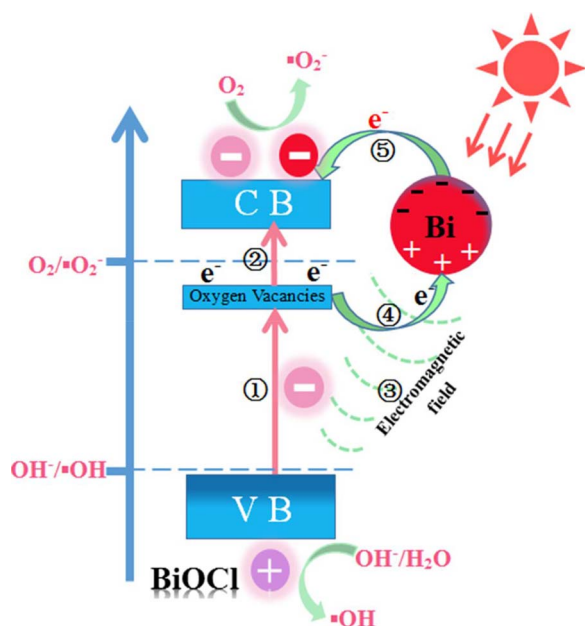
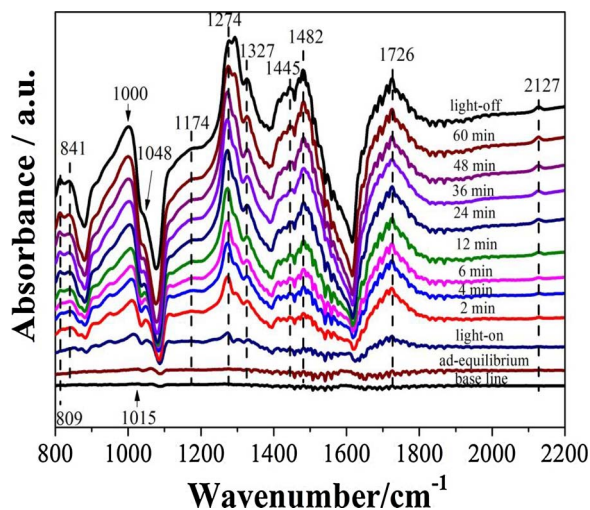**Fig. 8.** The mechanism of plasmonic photocatalysis on Bi/BiOCl-200.

Fig. 9. In situ FT-IR spectra of pho tocatalytic NO oxidation process over Bi/BiOCl-200 under visible light irradiation.

Table 2
Assignments of the IR bands observed during photocatalytic NO oxidation processes over Bi/BiOCl-200 under visible light irradiation.

Wave number (cm^{-1})	Band assignment	References
809,841	NO_3^-	60
1000	Bridging NO_3^-	62
1015,1048	Bidentate NO_3^-	60, 62
1174	Chelate NO_2^-	62
1274	N_2O_4	60
1327	NO_2^-	60
1445,1482	Bidentate NO_3^-	60
1726	N_2O_4	60
2127	NO^+	61, 63

accumulation of reaction products on the catalyst surface.

In order to further reveal the main active species in the photocatalytic reaction, the active species were captured with different trapping agents. Superoxide radicals ($\cdot O_2^-$), photogenerated electrons (e^-), hydroxyl radical ($\cdot OH$) and photogenerated hole (h^+) were

Table 3
The atomic content of Bi^{3+}, Bi^0, Cl, and O elements and the ratio of Bi to BiOCl of the samples determined from XPS data.

	Bi/BiOCl-180	Bi/BiOCl-200	Bi/BiOCl-210
Bi^{3+}	29.06%	58.88%	52.36%
Bi^0	10.06%	28.32%	34.84%
Cl	26.77%	6.24%	6.24%
O	34.12%	6.56%	6.56%
Bi^0/BiOCl	11.18%	39.51%	53.46%

captured by using 1, 4 benzoquinone (BQ), potassium dichromate ($K_2Cr_2O_7$), tert butyl alcohol (TBA) and potassium iodide (KI), respectively. Fig. 6d is shown that the activity of the sample mixed with $K_2Cr_2O_7$ is greatly inhibited. For other trapping agents, the activity of the sample is slightly decreased. These results indicate that photogenerated electrons (e^-) play a major role and other radicals play minor roles in the process of photocatalytic removal of NO.

3.5. Electrons delivery and photocatalysis mechanism

To further to recover the vital roles of Bi elements in Bi/BiOCl-200, we used the DFT to calculate the electronic structure of the catalysts. Fig. 7a shows the charge difference distribution of Bi elements on BiOCl. Charge accumulation is in blue and depletion in yellow. Obviously, the Bi-O layer of BiOCl attains abundant electrons from Bi elements and becomes the photo-active sites. The electronic location function (ELF) (Fig. 7b) demonstrates the existence of a strong covalent interaction between the Bi elements and Bi-O layer, forming a channel for hot electrons of Bi elements to transfer from Bi metals to BiOCl. In order to explore how the excited electrons of Bi can be easily transferred to the Bi-O layer, potentials of Bi/BiOCl and BiOCl were calculated. As showed in Fig. 7c, the potential of Bi elements is 26.14 eV higher than that of Bi-O layer. The energy barrier between Bi layer and Bi-O layer is only 6.99 eV. Under the visible light irradiation, excited hot electrons from Bi elements can easily cross the barrier and transfer to the adjacent Bi-O layer. From another aspect, we calculate the density of state (DOS) of Bi/BiOCl and BiOCl (Fig. 7d and e) and projected density of state (PDOS) of Bi element (Fig. 7f). Obviously, the valence-band maximum (VBM) of Bi/BiOCl is significantly extended by the contribution of the orbital from Bi element. This may be ascribed to the SPR effect of Bi elements urging the electrons of BiOCl to a higher excited state and gathering at the VBM [55]. This is beneficial to promote the generation of photogenerated charge carriers.

Based on the various experimental and theoretical results, the corresponding photocatalytic mechanism of Bi metal@defective BiOCl hierarchical microspheres mainly consists of five processes, as shown in Fig. 8. The oxygen vacancies in BiOCl induce the formation of intermediate level (Fig. 5d), allowing a direct transition from VB to intermediate level under visible light irradiation, as shown in process ①. This also enables the defective BiOCl with visible photocatalytic activity, because the electrons from the intermediate level can be further excited to the CB of BiOCl (process ②). Moreover, the introduction of Bi elements on BiOCl exerts a significant promotion effect on the visible light photocatalytic performance (Fig. 6c). First, the SPR effect of Bi elements produces the electromagnetic field to prompt the defective BiOCl with higher excited state electrons gathering at the VBM, which in favour of the separation of the photogenerated electron-hole pairs (process ③). Second, hot electrons of Bi elements transfer to Bi-O layer (process ⑤) and the electrons from the intermediate level transfer to Bi elements to maintain neutrality of Bi elements at the same time (process ④), which promote the electron-hole pairs separation of BiOCl and increase the radical production. Hence, by in situ reduction of Bi^{3+} to Bi elements and creation of defects on hierarchical microsphere structure of BiOCl, the photocatalytic performance can be significantly improved.
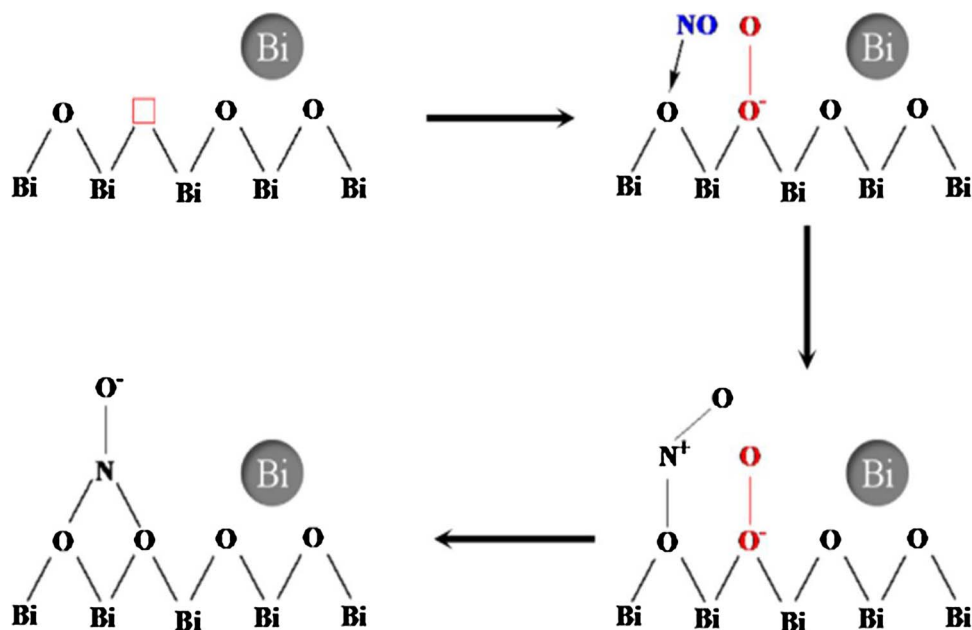
Scheme 1. A possible mechanism of NO adsorption on Bi/BiOCl-200.
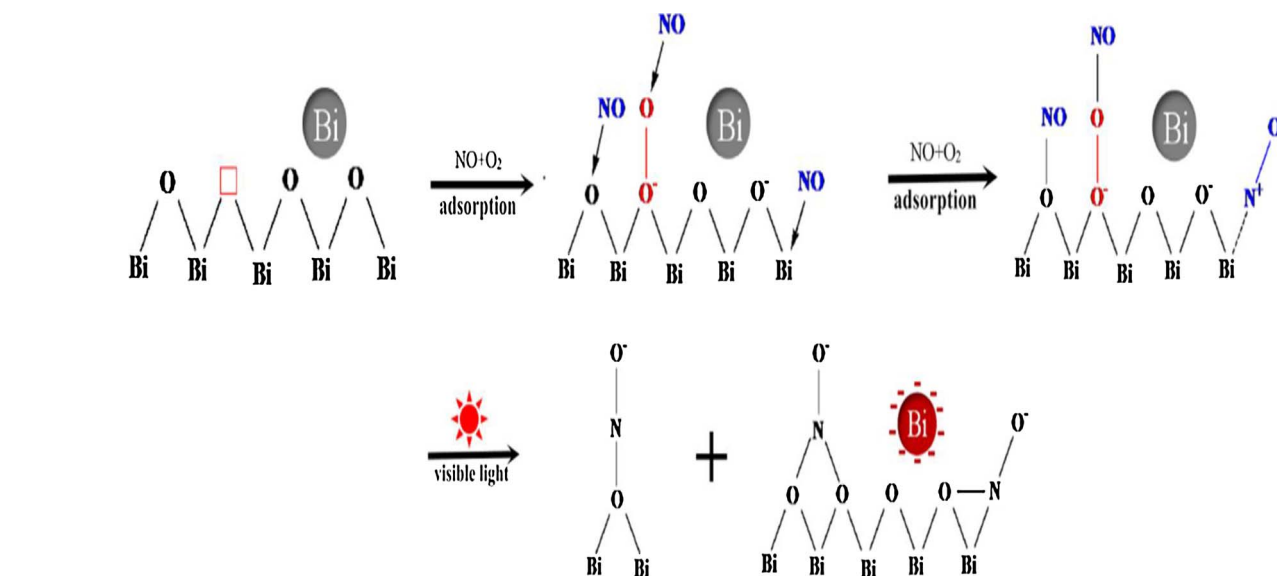
Scheme 2. A possible mechanism of photocatalytic NO oxidation on Bi/BiOCl-200.
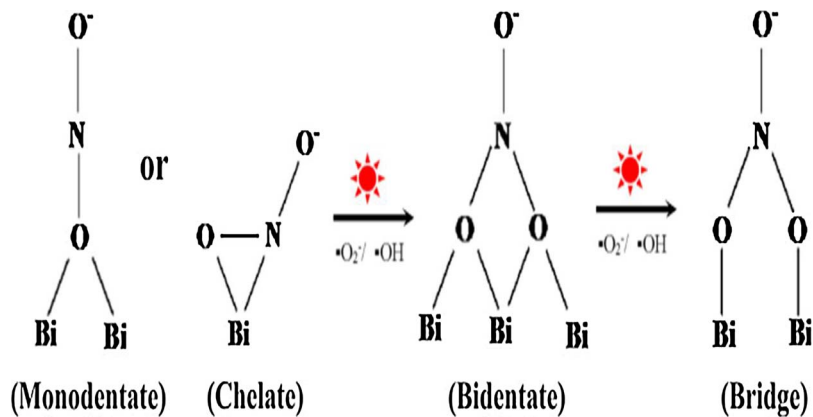
Scheme 3. A possible mechanism of nitrates oxidation on Bi/BiOCl-200.

(Monodentate)   (Chelate)   (Bidentate)   (Bridge)

3.6. In situ FT-IR investigation on the photocatalytic reaction mechanism

Fig. 9 displays the in-situ FTIR spectra of the NO adsorption in the dark and photocatalytic reaction processes on the surface of Bi/BiOCl-200 under visible light irradiation. Table 2 summarizes the assignment of the corresponding absorption bands. Under dark condition, the absorption peak of nitrates (1048 cm^{-1}) is noted after adsorption equilibrium. This could attribute to oxygen vacancies in BiOCl that could activate the adsorbed O_2 to form superoxide radical ($\cdot O_2^-$), oxidizing the NO to nitrates [56]. A proposed workable mechanism of NO adsorption is illustrated in Scheme 1.

After visible light irradiation, enhanced absorption bands of the NO_2 polymer (N_2O_4), nitrites (at 1174 and 1327 cm^{-1}) and nitrates (at 809, 841, 1000, 1015, 1048, 1445 and 1482 cm^{-1}) can be detected. This is indicative of the active species generated under visible light that induces the photocatalytic NO oxidation, consisting with the transient decrease in NO concentration after visible light for the first 2 min in Fig. 6c. As for the photocatalytic reaction progresses, the absorption peaks of different forms of nitrites and nitrates are corresponding generation, which may be due to the NO adsorbed at diverse locations on the surface of the photocatalyst (as shown in Scheme 2). In addition, nitrites and nitrates tend to be oxidized to the more stable state by superoxo species[57]. Hence, the absorption peak at 1015 cm^{-1} (Bidentate NO_3^-) gradually shifts to 1000 cm^{-1} (Bridging NO_3^-) with the increase of the illumination time (as shown in Scheme 3). It is worth to note that the absorption bands located at 2127 cm^{-1} can be attributed to the nitrosonium ion (NO^+), which is derived from NO oxidized by the photogenerated holes with strongly oxidative properties[58–63]. However, the absorption peak of the NO^+ is always weak. The reason for this result is that the anionic $\cdot O_2^-$ preferentially oxidize cationic NO^+ into nitrites or nitrates. Therefore, the formation of NO^+ could promote the NO photocatalytic oxidization [59,60,64].

4. Conclusion

In this work, plasmonic Bi metal@defective BiOCl with 3D hierarchal structure was constructed by a one-step solvothermal method. The visible light photocatalytic NO purification on the plasmonic Bi metal@defective BiOCl was greatly improved. This is primarily attributed to the co-effects of oxygen vacancies and Bi metals. Oxygen vacancies induced the formation of intermediate level to realize the transition of photogenerated electron-hole pairs under visible light irradiation and Bi metals could promote the charge carriers separation efficiency, providing more hot electrons to increase the production of radicals. The reaction process of photocatalytic oxidation NO was systematically studied by in situ FTIR. The NO was adsorbed on the surface of photocatalysts at different locations, and would be oxidized to diverse forms of nitrite and nitrate. Combining the radical capture, DFT calculation and the reaction process, the relevant reaction mechanism of photocatalytic oxidation NO on Bi metal@defective BiOCl was proposed involving the important roles of synergistic roles of oxygen vacancies and Bi metal. This study provides a new method for the design of non-noble metal-based photocatalysts, and offers a new method to understand the gas phase photocatalytic reaction mechanism, as well as the mechanisms of SPR effect and defects synergistically enhance the photocatalytic performance.

Acknowledgements

Appendix A. Supplementary data

Supplementary data associated with this article can be found, in the online version, at https://doi.org/10.1016/j.apcatb.2017.11.079.

References

[1] L. Zhang, W. Wang, J. Yang, Z. Chen, W. Zhang, L. Zhou, S. Liu, Sonochemical synthesis of nanocrystallite Bi_2O_3 as a visible-light-driven photocatalyst, Appl. Catal. A 308 (2006) 105–110.
[2] P.D. Battle, C.R.A. Catlow, J. Drennan, A.D. Murray, The structural properties of the oxygen conducting delta-phase of Bi_2O_3, J. Phys. C Solid State Phys. 16 (1983) 561–566.
[3] Z.Y. Jiang, X.H. Liang, H.L. Zheng, Y.Y. Liu, Z.Y. Wang, P. Wang, X.Y. Zhang, X.Y. Qin, Y. Dai, M.H. Wangbo, B.B. Huang, Photocatalytic reduction of CO_2 to methanol by three-dimensional hollow structures of Bi_2WO_6 quantum dots, Appl. Catal. B 219 (2017) 209–215.
[4] C.M. Li, G. Chen, J.X. Sun, J.C. Rao, Z.H. Han, Y.D. Hu, W.N. Xing, C.M. Zhang, Doping effect of phosphate in Bi_2WO_6 and universal improved photocatalytic activity for removing various pollutants in water, Appl. Catal. B 188 (2016) 39–47.
[5] Z. Zhang, W. Wang, S. Meng, W. Yin, Low-temperature combustion synthesis of Bi_2WO_6 nanoparticles as a visible-light-driven photocatalyst, J. Hazard. Mater. 177 (2010) 1013–1018.
[6] G. Tian, Y. Chen, W. Zhou, K. Pan, Y. Dong, C. Tian, H. Fu, Facile solvothermal synthesis of hierarchical flower-like Bi_2MoO_6 hollow spheres as high performance visible-light driven photocatalysts, J. Mater. Chem. 21 (2010) 887–892.
[7] J. Bi, L. Wu, J. Li, Z. Li, X. Wang, X. Fu, Simple solvothermal routes to synthesize nanocrystalline Bi_2MoO_6 photocatalysts with different morphologies, Acta Mater. 55 (2007) 4699–4705.
[8] L. Zhang, T. Xu, X. Zhao, Y. Zhu, Controllable synthesis of Bi_2MoO_6 and effect of morphology and variation in local structure on photocatalytic activities, Appl. Catal. B 98 (2010) 138–146.
[9] M. Long, P.D. Hu, H.D. Wu, J. Cai, B.H. Tan, B.X. Zhou, Efficient visible light photocatalytic heterostructure of nonstoichiometric bismuth oxyiodide and iodine intercalated $Bi_2O_2CO_3$, Appl. Catal. B 184 (2016) 20–27.
[10] H. Cheng, B. Huang, K. Yang, Z. Wang, X. Qin, X. Zhang, Y. Dai, Facile template-free synthesis of $Bi_2O_2CO_3$ hierarchical microflowers and their associated photocatalytic activity, ChemPhysChem 11 (2010) 2167–2173.
[11] L.Y. Ding, R.J. Wei, H. Chen, J.C. Hu, J.L. Li, Controllable synthesis of highly active BiOCl hierarchical microsphere self-assembled by nanosheets with tunable thickness, Appl. Catal. B 173 (2015) 91–99.
[12] M. Shang, W. Wang, L. Zhang, Preparation of BiOBr lamellar structure with high photocatalytic activity by CTAB as Br source and template, J. Hazard. Mater. 167 (2009) 803–809.
[13] A. Luz, C. Feldmann, Phase-transfer assisted synthesis of BiOI nanoplatelets, quantum-confined color and selective modification of surface conditioning, Solid State Sci. 13 (2011) 1017–1021.
[14] M. Ou, F. Dong, W. Zhang, Z. Wu, Efficient visible light photocatalytic oxidation of NO in air with band-gap tailored $(BiO)_2CO_3$@BiOI solid solutions, Chem. Eng. J. 255 (2014) 650–658.
[15] Y. Sun, X. Xiao, X. Dong, F. Dong, Wei Zhang, Heterostructured BiOI@La(OH)$_3$ nanorods with highly enhanced visible light photocatalytic NO removal, Chin. J. Catal. 38 (2017) 217–226.
[16] T. Xiong, H. Huang, Y. Sun, F. Dong, In-situ synthesis of a C-doped $(BiO)_2CO_3$ hierarchical self-assembly effectively promoting visible light photocatalysis, J. Mater. Chem. A 3 (2015) 6118–6127.
[17] F. Dong, Y. Sun, M. Fu, W.K. Ho, S.C. Lee, Z. Wu, Novel in situ N-doped $(BiO)_2CO_3$ hierarchical microspheres self-assembled by nanosheets as efficient and durable visible light driven photocatalyst, Langmuir 28 (2012) 766–773.
[18] J. Toudert, R. Serna, M.J.D. Castro, Exploring the optical potential of nano-bismuth: tunable surface plasmon resonances in the near ultraviolet-to-near infrared range, J. Phys. Chem. C 116 (2012) 20530–20539.
[19] Z. Ni, W. Zhang, G. Jiang, X.g Wang, Z. Lu, Y. Sun, X. Li, Y. Zhang, F. Dong, Enhanced plasmonic photocatalysis of SiO_2@Bi microspheres with hot electrons transportation channel via Bi-O-Si linkage, Chin. J. Catal. 38 (2017) 1174–1183.
[20] F. Dong, T. Xiong, Y. Sun, Z. Zhao, Y. Zhou, X. Feng, Z. Wu, A semimetal bismuth element as a direct plasmonic photocatalyst, Chem. Commun. 50 (2014) 10386–10389.
[21] Z. Zhao, W. Zhang, X. Lv, Y. Sun, F. Dong, Y. Zhang, Noble metal-free Bi nanoparticles supported on TiO_2 with plasmon-enhanced visible light photocatalytic air purification, Environ. Sci. Nano 3 (2016) 1306–1317.
[22] F. Dong, Z. Zhao, Y. Sun, Y. Zhang, S. Yan, Z. Wu, An advanced semimetal–organic Bi spheres–g-C_3N_4 nanohybrid with SPR-enhanced visible-light photocatalytic performance for NO purification, Environ. Sci. Technol. 49 (2015) 12432–12440.
[23] F. Dong, Q. Li, Y. Sun, W.K. Ho, Noble metal-like behavior of plasmonic Bi particles as a cocatalyst deposited on $(BiO)_2CO_3$ microspheres for efficient visible light photocatalysis, ACS Catal. 4 (2014) 4341–4350.
[24] Y.K. Huang, S.F. Kang, Y. Yang, H.F. Qin, Z.J. Ni, S.J. Yang, X. Li, Facile synthesis of Bi/Bi_2WO_6 nanocomposite with enhanced photocatalytic activity under visible light, Appl. Catal. B 196 (2016) 89–99.
[25] C. Chang, L. Zhu, Y. Fu, X. Chu, Highly active Bi/BiOI composite synthesized by one-step reaction and its capacity to degrade bisphenol A under simulated solar light irradiation, Chem. Eng. J. 233 (2013) 305–314.
[26] Y. Yu, C. Cao, H. Liu, P. Li, F. Wei, Y. Jiang, W. Song, A Bi/BiOCl heterojunction

photocatalyst with enhanced electron-hole separation and excellent visible light photodegrading activity, J. Mater. Chem. A 2 (2014) 1677–1681.

[27] S. Weng, B. Chen, L. Xie, Z. Zheng, P. Liu, Facile in situ synthesis of a Bi/BiOCl nanocomposite with high photocatalytic activity, J. Mater. Chem. A 1 (2013) 3068–3075.

[28] F. Dong, T. Xiong, S. Yan, H. Wang, Y. Sun, Y. Zhang, H. Huang, Z. Wu, Facets and defects cooperatively promote visible light plasmonic photocatalysis with Bi na-nowires@BiOCl nanosheets, J. Catal. 344 (2016) 401–410.

[29] T. Weiland, A discretization model for the solution of Maxwell's equations for six-component fields, Archiv Elektronik Und Uebertragungstechnik 31 (1977) 116–120.

[30] C. Pflaum, Z. Rahimi, An iterative solver for the finite-difference frequency-domain (FDFD) method for the simulation of materials with negative permittivity, Numer Linear Algebr 18 (2011) 653–670.

[31] S. Yan, J. Krantz, K. Forberich, C. Pflaum, C.J. Brabec, Numerical simulation of light propagation in silver nanowire films using time-harmonic inverse iterative method, J. Appl. Phys. 113 (2013) 689–698.

[32] H. Hagemann, W. Gudat, C. Kunz, Deutsches Elektronensynchrotron Hamburg, Report No. DESYSR-74-7 (unpublished), (1974).

[33] H. Nakai, J. Heyd, G.E. Scuseria, Periodic-boundary-condition calculation using heyd-scuseria-ernzerh of screened coulomb hybrid functional: electronic structure of anatase and rutile TiO$_2$, J. Chem. Softw. 5 (2006) 7–18.

[34] G. Kresse, J. Furthmüller, Efficiency of abinitio total energy calculations for metals and semiconductors using a plane-wave basis set, Comput. Mater. Sci. 6 (1996) 15–50.

[35] G. Kresse, J. Furthmüller, Efficient iterative schemes for ab initio total-energy cal-culations using a plane-wave basis set, Phys. Rev. B 54 (1996) 11169–11186.

[36] J.P. Perdew, K. Burke, M. Ernzerhof, Generalized gradient approximation made simple, Phys. Rev. Lett. 77 (1996) 3865–3868.

[37] B.P.E, Projector augmented-wave method, Phys. Rev. B 50 (1994) 17953–17979.

[38] G. Kresse, D. Joubert, From ultrasoft pseudopotentials to the projector augmented-wave method, Phys. Rev. B 59 (1999) 1758–1775.

[39] S.K. Bhatia, A.L. Myers, Optimum conditions for adsorptive storage, Langmuir 22 (2006) 1688–1700.

[40] R.C. Lochan, M. Head-Gordon, Computational studies of molecular hydrogen binding affinities: the role of dispersion forces, electrostatics, and orbital interac-tions, Phys. Chem. Chem. Phys. 8 (2006) 1357–1370.

[41] J. Jiang, L. Zhang, H. Li, W. He, J.J. Yin, Self-doping and surface plasmon mod-ification induced visible light photocatalysis of BiOCl, Nanoscale 5 (2013) 10573–10581.

[42] F. Dong, T. Xiong, Y. Sun, H. Huang, Z. Wu, Synergistic integration of thermo-catalysis and photocatalysis on black defective (BiO)$_2$CO$_3$ microspheres, J. Mater. Chem. A 3 (2015) 18466–18474.

[43] Y. Fujimoto, New Infrared Luminescence from Bi-doped Glasses, InTech, 2010.

[44] F. Dong, Y. Sun, M. Fu, Z. Wu, S.C. Lee, Room temperature synthesis and highly enhanced visible light photocatalytic activity of porous BiOI/BiOCl composites nanoplates microflowers, J. Hazard. Mater. 26 (2012) 219–220.

[45] Z. Ai, W. Ho, S. Lee, L. Zhang, Efficient photocatalytic removal of NO in indoor air with hierarchical bismuth oxybromide nanoplate microspheres under visible light, Environ. Sci. Technol. 43 (2009) 4143–4150.

[46] I. Nakamura, N. Negishi, S. Kutsuna, T. Ihara, S. Sugihara, K. Takeuchi, Role of oxygen vacancy in the plasma-treated TiO$_2$ photocatalyst with visible light activity for NO removal, J. Mol. Catal. A: Chem. 161 (2000) 205–212.

[47] L. Ye, L. Zan, L. Tian, T. Peng, J. Zhang, The {001} facets-dependent high photo-activity of BiOCl nanosheets, Chem. Commun. 47 (2011) 6951–6953.

[48] Z. Diwu, J.W. Lown, EPR studies of photodynamic action of hypericin: formation of semiquinone radical and activated oxygen species on illumination, Free Radic. Biol. Med. 14 (1993) 209–215.

[49] M. Ikeya, Dating a stalactite by electron paramagnetic resonance, Nature 255 (1975) 48–50.

[50] T. Stauber, N.M.R. Peres, F. Guinea, Electronic transport in graphene: a semi-clas-sical approach including midgap states, Phys. Rev. B 76 (2007) 205423–205433.

[51] J. Ke, J. Liu, H. Sun, H. Zhang, X. Duan, P. Liang, X. Li, M.O. Tade, S. Liu, S. Wang, Facile assembly of Bi$_2$O$_3$/Bi$_2$S$_3$/MoS$_2$ *n*-pheterojunction with layered *n*-Bi$_2$O$_3$ and *p*-MoS$_2$ for enhanced photocatalytic water oxidation and pollutant degradation, Appl. Catal. B—Environ. 200 (2017) 47–55.

[52] Q. Zhao, Y. Ren, X. Li, Y. Shi, Photo-induced activity of BiFeO$_3$/TiO$_2$ nanotube arrays derived from ultrasound-assisted successive ionic layer adsorption and re-action, Mater. Res. Bull. 83 (2016) 396–399.

[53] F. Zhang, X. Li, Q. Zhao, A. Chen, Facile and controllable modification of 3D In$_2$O$_3$ microflowers with In$_2$S$_3$ nanoflakes for efficient photocatalytic degradation of gaseous *ortho*-dichlorobenzene, J. Phys. Chem. C 120 (34) (2016) 19113–19123.

[54] Y. Sun, Z. Zhao, F. Dong, W. Zhang, Mechanism of visible light photocatalytic NOx oxidation with plasmonic Bi cocatalyst-enhanced (BiO)$_2$CO$_3$ hierarchical micro-spheres, Phys. Chem. Chem. Phys. 17 (2015) 10383–10390.

[55] H. Li, J. Shang, H. Zhu, Z. Yang, Z. Ai, L. Zhang, Oxygen vacancy structure asso-ciated photocatalytic water oxidation of BiOCl, ACS Catal. 6 (2016) 8276–8285.

[56] J. Li, S. Yin, F. Dong, W. Cen, Y. Chu, Tailoring active sites via synergy between graphitic and pyridinic N for the enhanced catalytic efficiency of carbocatalyst, ACS Appl. Mater. Interfaces 9 (2017) 19861–19869.

[57] K.I. Hadjiivanov, Identification of neutral and charged NxOy surface species by IR spectroscopy, Catal. Rev. 42 (2000) 71–144.

[58] J.C.S. Wu, T. Cheng, In situ FTIR study of photocatalytic NO reaction on photo-catalysts under UV irradiation, J. Catal. 237 (2006) 393–404.

[59] L. Zhong, Y. Yu, W. Cai, X. Geng, Q. Zhong, Structure-activity relationship of Cr/Ti-PILC catalysts using a pre-modification method for NO oxidation and their surface species study, Phys. Chem. Chem. Phys. 17 (2015) 15036–15045.

[60] N. Tang, Y. Liu, H. Wang, Z. Wu, Mechanism study of NO catalytic oxidation over MnOx/TiO$_2$ catalysts, J. Phys. Chem. C 115 (2011) 8214–8220.

[61] L. Jaan, J.R. Ohlsen, Characterization of Nitrogen Oxides by Vibrational Spectroscopy, (2007).

[62] K. Hadjiivanov, V. Avreyska, A. Dimitar Klissurski, T. Marinova, Surface species formed after NO adsorption and NO + O$_2$ coadsorption on ZrO$_2$ and sulfated ZrO$_2$: an FTIR spectroscopic study, Langmuir 18 (2012) 1619–1625.

[63] J. Valyon, W.K. Hall, Studies of the surface species formed from nitric oxide on copper zeolites, J. Phys. Chem. 97 (1993) 1204–1212.

[64] X. Feng, W. Zhang, Y. Sun, H. Huang, F. Dong, Fe(III) clusters-grafted (BiO)$_2$CO$_3$ superstructures: in situ DRIFTS investigation on IFCT-enhanced visible light pho-tocatalytic NO oxidation, Environ. Sci. Nano 4 (2017) 604–612.